BL14C/2011G672,BL14B2013G731

Crystal Analyser-based X-ray Phase Contrast Imaging in the Dark Field: Implementation and Evaluation using Excised Tissue Specimens

Masami Ando[1], Naoki Sunaguchi[2], Synho Do[3], Yongjin Sung[3], Abner Louissaint[3], Wu Yanlin[4], Tetsuya Yuasa[5], Yoshifumi Suzuki[6], Shu Ichihara[7], Rajiv Gupta[3*]

[1]Tokyo University of Science, Noda, Chiba 278-8510, Japan
[2]Gunma University, Kiryu, Gunma 376-8515, Japan
[3]Massachusetts General Hospital and Harvard Medical School, Boston, MA 02114, USA
[4]Graduate University for Advanced Studies, Tsukuba, Ibaraki 305-0801, Japan
[5]Yamagata University, Yonezawa, Yamagata, 992-8510, Japan
[6]Kyushu Institute of Technology, Kitakyushu, Fukuoka, 804-8550, Japan
[7]Nagoya Medical Center, Nagoya, Aichi 460-001, Japan

1 Introduction

X-ray absorption, arising primarily from photoelectric absorption and Compton scattering, is markedly different in bones, soft tissues and air, but very similar among different soft tissue types [1]. X-ray phase imaging (XPI) records coherent scattering or refraction of light due to the electron density differences in an object [2]; therefore, it can image soft tissues with much higher contrast resolution than traditional radiography. X-ray dark field imaging (XDFI) adopts a thin crystal in transmission Laue mode, and thus can detect the angular deviation on the order of 10^{-4} – 10^{-5} degrees [3]. In this report, we describe the most recent advancements in XDFI and apply it to a variety of human tissue specimens. Specifically, we reduce the thickness of the analyser crystal to 150 μm, and adopt an asymmetric-cut monochromator-collimator. The phase images obtained with the proposed XDFI system clearly demonstrate soft tissue discrimination capability in various specimens.

2 Experiment

The experimental setup for XDFI and the associated optics are schematically shown in Fig. 1. The setup comprises an X-ray source, an asymmetrically-cut Bragg-type monochromator-collimator (MC), a Laue-case angle analyser (LAA) and two CCD cameras. The specimen is placed between the MC and the LAA. For the light source, we used a synchrotron radiation, the beamline BL14C on a 2.5 GeV storage ring (KEK Photon Factory, Tsukuba, Japan). The magnetic field of a 5-T superconducting wiggler is horizontally orientated, which provides the vertically-polarised X-ray beam. The (440) atomic planes of the MC are vertically aligned so that the plane of incidence is horizontal. This enables the entire system to be placed on a horizontal optical table. MC provides a quasi-monochromatic X-ray beam with narrow bandwidth ($\Delta\lambda/\lambda = 2.9 \times 10^{-4}$) and small-divergence, both of which are critical for the high angular selectivity of XDFI. By adopting an MC with an asymmetric cut, the beam can be expanded up to 60 mm vertically and 70 mm horizontally to perform full-field imaging of a large specimen. The asymmetric factor of MC is determined by $b = \sin(\Theta_B-\alpha)/\sin(\Theta_B+\alpha)$ where Θ_B is the Bragg angle and α is the asymmetry angle between the crystal surface and the diffracting planes. For the results included in this study, we have used the following values: $\Theta_B = 12.0^o$ (440 diffraction at 31 keV), $\alpha = 11.1^o$, and thus $b = 0.04$. The sample plane is located 38 m away from the source, and the CCD camera is at 0.7 m from the sample. The spatial resolution given by the Takagi-Taupin equation [4-6] is 1.3 μm and 4 μm in the vertical and horizontal directions, respectively. We note that these values can be further improved by narrowing the wavelength spread and by thinning the LAA down to 100 μm or less. XDFI can be performed in a high-speed mode using two cameras, which record forward diffraction (FD) and diffraction (D) images simultaneously. Alternatively, in this study we used a single camera to record the FD and D images sequentially. The CCD camera (X-FDI 1.00:1, Photonic Science Ltd.) used for the recording has a 7.4-μm pixel size and a reasonably large field of view (36.1 mm (h) x 24.0 mm (v)). The CCD chips have 16-bit dynamic range and are air-cooled. For phase contrast computed tomography, we mount each specimen on a precision rotational stage and obtain two sets (FD and D) of images (600 images each) while rotating the specimen around a vertical axis. The angular interval is 0.3°, and the angular span is 180°. A detailed description on the tomographic reconstruction algorithm can be found in [7].

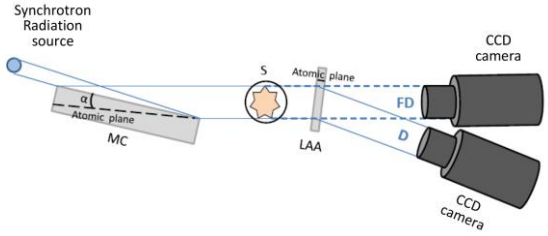

Fig. 1: Schematic diagram of the experimental set-up.

3 Results and Discussion

Using XDFI, we have imaged the anterior chamber of an enucleated eye. The sagittal slices of the reconstructed differential phase map (Figs. 2A (i)-(iv)) show markedly increased detail and contrast, especially at the interfaces. These images clearly demonstrate the margins of the cornea, iris, pupil, ciliary body, angle, lens, and the

suspensory ligament of the lens. These differential phase images were converted into the refractive index images in the coronal and sagittal (Figs. 2B (i) and (ii), respectively) planes where the same structures can be visualised. For comparison, the anterior chamber of the same specimen, imaged using standard multidetector CT (MDCT) , and H&E (haematoxylin and eosin) staining are shown in Figs. 2B (iii) and (iv), respectively. We have also imaged the posterior globe and the site of optic nerve insertion of the same specimen using XDFI. Fig. 2C clearly shows the tri-laminar structure of the globe consisting of the retina, the choroid and the sclera. The insertion of the optic nerve into the globe is clearly shown along with the central retinal artery, the nerve fascicles and the optic nerve sheath which is contiguous with the sclera. The dark-field CT slice through the globe also shows separation of the retinal and choroidal layers from the underlying sclera at multiple places. This may be due to the post-mortem condition, prolonged formalin-fixation, and contraction of the vitreous humour. Irrespective of the aetiology, the retinal and choroidal detachments are well demonstrated by XDFI. In fact, the phase contrast image can show whether only one or both layers are involved. The histology images confirm the presence of retinal and choroidal detachment. The histological processing of the specimen likely worsened the detachment of the retina and the choroid, as can be seen in Fig. 2C, where it extends up to the optic nerve insertion.

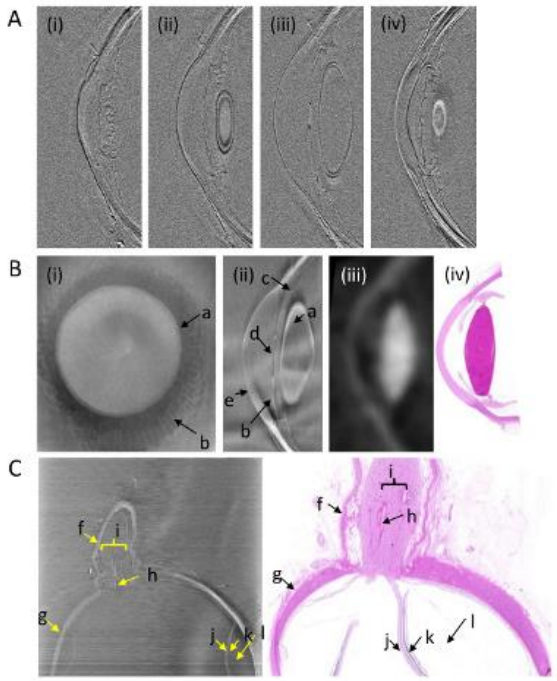

Fig. 2: Anterior and posterior chambers of an eyeball imaged with XDFI. (A) Tomographic slices (sagittal plane) of the differential phase map of an anterior chamber ((i)-(iv)). (B) Refractive index images in the coronal (i) and sagittal (ii) planes, a matched absorption image from conventional MDCT (iii), and a histological H&E slide showing this specimen (iv); the difference in the imaging and histological appearance are due to tissue retraction during histological processing and sample preparation. (C) Globe and optic nerve insertion of the same specimen. a: lens; b: iris muscle; c: ciliary body; d. pupil; e. cornea; f. optic nerve sheath; g. sclera; h. central retinal artery; i. nerve fascicles; j. retina; k. choroid; l. sub-choroidal space.

We also applied XDFI and MDCT to a heavily diseased iliac artery containing atherosclerotic plaque. Figure 3 shows the absorption and phase tomographic slices from XDFI (Fig. 3(i) and 3(ii)), an approximately matched CT image from an MDCT system (Fig. 3(iii)), and the corresponding histopathology slide (Fig. 3(iv)). As can be clearly seen in Fig. 3(i), the absorption image (Fig. 3(i)) shows only calcifications in this atherosclerotic plaque specimen. The phase image (Fig. 3(ii)), on the other hand, shows a lot of detail of the atherosclerotic plaque components. For example, the tri-laminar structure of the vessel wall consisting of the adventitia, the media and the intima can be appreciated. In addition, the intima, which is contiguous with the fibrous cap over the atheroma within the plaque, is clearly visualised. These structures are distinct from the calcification which shows artefacts from a phase saturation effect. The phase shift value of the round plastic rod placed adjacent to the specimen is highly uniform, which shows the fidelity of our method. The details seen on the phase image of plaque morphology are well matched with the corresponding histology slide (Fig. 3(iv)).

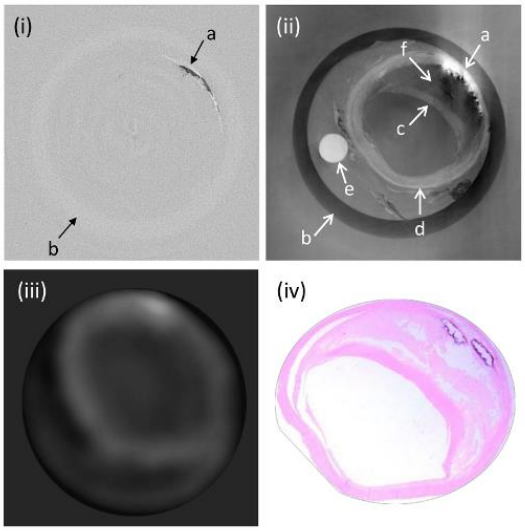

Fig. 3: An iliac artery specimen with atherosclerotic plaque. Absorption (i) and phase (ii) tomographic slices from XDFI, a matched CT slice from MDCT (iii), and the corresponding H&E-stained histopathology slide (iv). a: calcification; b: plastic container; c: fibrous cap; d: three-layer arterial wall; e: plastic rod; and f: soft plaque.

Using XDFI, we have imaged breast biopsy specimens containing both benign and malignant tumours. Fig. 4A shows radiological and histological images from the case of a 33-year-old woman with a small breast mass and bloody nipple discharge. Before sectioning using standard

histopathology techniques, the paraffin-embedded surgical specimen from an excisional biopsy was imaged using XDFI. The absorption image (Fig. 4A(i)) from XDFI reveals no significant contrast between the various tissue types in the specimen except for a focus of amorphous microcalcification. The phase image (Fig. 4A(ii)), on the other hand, shows a prominent terminal duct lobular unit (TDLU) distinct from the surrounding breast parenchyma. Changes in the lobular morphology are better seen in the magnified view (Fig. 4A(iv)), which shows the breast TDLU with the increased number and size of the glandular tissue. The enlarged units maintain a lobulocentric arrangement without any evidence of infiltration beyond the margins. These findings were confirmed on histopathology as shown in Fig. 4A(iii and v), in which a diagnosis of benign nodular adenosis was made. Fig. 4B shows another benign breast tumour in a 42-year-old woman whose slowly enlarging mass was surgically removed. The phase image (Fig. 4B(i)) shows well-demarcated, homogeneous tissue compressing the normal ducts and the TDLU. The histopathology, shown in Fig. 4B(ii), confirmed the diagnosis of a phyllodes tumour, a circumscribed fibroepithelial neoplasm composed of a double-layered epithelial component and a hypercellular stromal component.

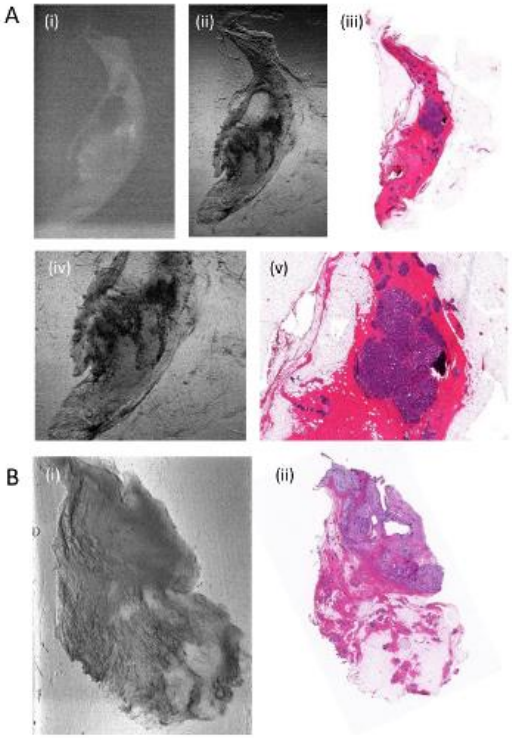

Fig. 4: Breast tissue excisional biopsy specimens with benign tumours. (A) Specimen from a 33-year-old woman with a small breast mass and bloody nipple discharge: (i) absorption; (ii) phase; and (iii) a matched H&E-stained slide. Panels (iv) and (v) are zoomed-in views of (ii) and (iii), respectively. (B) Tissue specimen from a 42-year-old woman with a long-term follow up of a slowly enlarging mass that was surgically removed: (i) phase image and (ii) H&E-stained histopathology slide.

Fig. 5A shows the case of a 54-year-old woman with discharge from the left nipple. Mammography revealed heterogeneous dense breast parenchyma with suspicious microcalcifications. The absorption image (Fig. 5A(i)) of the excisional biopsy specimen is inconclusive because of poor soft tissue contrast. The phase image (Fig. 5A(ii)) has a suggestion of dilated, epithelial-lined structures containing hyperintense or hyper-refractive material. This finding was confirmed by pathology (Fig. 5A(iii)) which yielded the diagnosis of a high-grade ductal carcinoma in situ (DCIS) with comedo-type necrosis. Fig. 5B shows another case of DCIS in a 37-year-old woman who presented with a palpable stiffness in the left breast. Standard mammographic views showed a focal asymmetric density with only faint and unclear microcalcifications in this area. These calcifications were better demonstrated on the absorption image, Fig. 5B(i), from XDFI. The phase image (Fig. 5B(ii)) shows hyperintense material in dilated ducts that is also consistent with a high-grade DCIS with comedo-type necrosis, a diagnosis confirmed by pathology (Fig. 5B(iii)). The phase contrast images of the DCIS are consistent with those obtained with diffraction enhanced imaging (DEI) CT [7].

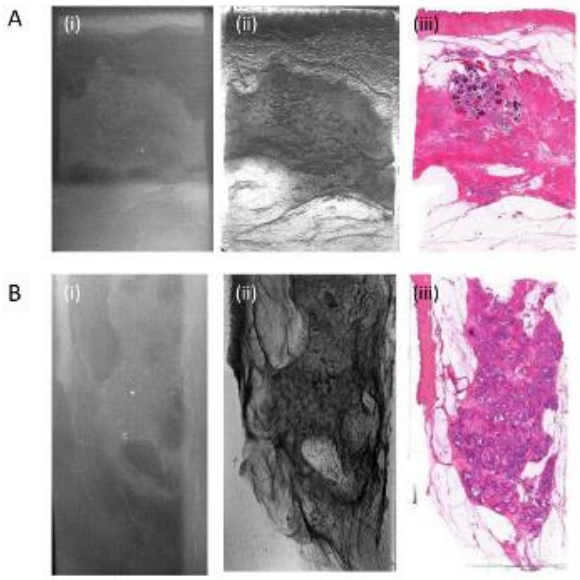

Fig. 5: Breast tissue specimens with ductal carcinoma in situ (DCIS). (A) Specimen from a 54-year-old woman with discharge from the left nipple: (i) absorption; (ii) phase images; and (iii) a matched H&E-stained slide. (B) A second specimen from a different patient with the same pathological condition: a 37-year-old woman with a palpable stiffness in the left breast; (i) absorption; (ii) phase images; and (iii) a matched H&E-stained slide.

Figs. 6A and 6B show examples of invasive carcinoma in two different patients. The first patient (Fig. 6A), a 38-year-old woman with left breast stiffness, demonstrated an infiltrating mass on mammography and MRI. The phase contrast image (Fig. 6A(i)) shows an expansile

lesion that permeates the breast parenchyma, with preserved normal TDLU and multiple cysts, an appearance confirmed by histopathology (Fig. 6A(ii)) where a diagnosis of invasive carcinoma of no special type was made. Fig. 6B shows a phase image and the corresponding histopathology images from a 45-year-old woman with right nipple haemorrhagic discharge and multifocal breast tumour with infiltration of the nipple. The infiltrative nature of the tumour, with adjacent skin invasion is well demonstrated on both the phase image Fig. 6B(i) as well as the histopathology slide (Fig. 6B(ii)).

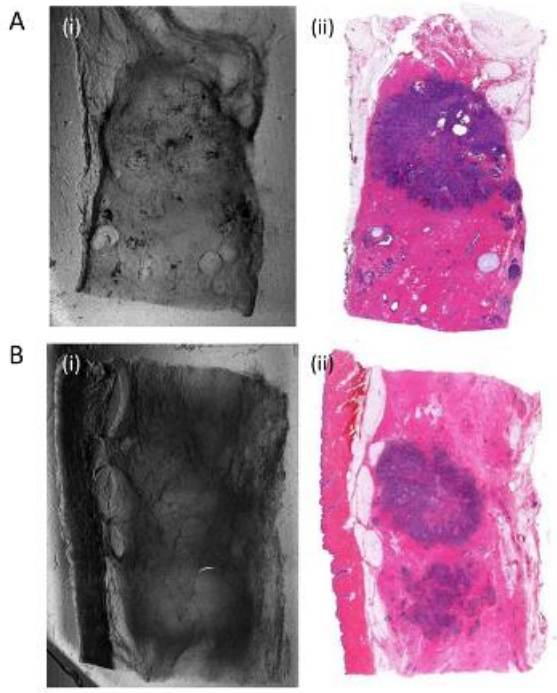

Fig. 6: Infiltrating breast carcinoma. (A) Tissue specimen from a 38-year-old woman with left breast stiffness: (i) phase image; and (ii) H&E-stained histopathology slide. (B) Another case of an infiltrating carcinoma from a 45-year-old woman with right nipple haemorrhagic discharge and tumour infiltration of the nipple: (i) phase image; and (ii) H&E-stained slide. In both cases, normal phase signature of the breast parenchyma has been replaced by relatively homogeneous tumour cells; in the second case, also note the skin thickening and altered phase signature of the cutaneous/subcutaneous regions due to tumour infiltration.

Acknowledgement

The authors would like to thank Mr. Kazuki Matsui, Ms Megumi Yokoyama and Ms Mayumi Kataoka for their technical assistance, and Dr. Suzuko Moritani and Dr. Masaki Hasegawa for providing clinicopathological data. Valuable help in sample preparation and imaging was provided by Drs. Suzanne Lee, Kazuyuki Hyodo, Qingkai Huo, Ms. Andrea Schmitz and Mr. Yuki Nakao. This work was supported, in part, by the DARPA AXiS program, Grant Number: N66001-11-4204, P.R. Number: 1300217190. This research was also supported, in part, by a Grant-in-Aid for Scientific Research (No. 22591353) from the Ministry of Education, Culture, Sports, Science and Technology (MEXT) in Japan, and in part by a Grant-in-Aid for Clinical Research from the National Hospital Organization. This report is excerpted from the manuscript which was published in European Radiology [9].

References

[1] Photon, Electron, Proton and Neutron Interaction Data for Body Tissues, ICRU Report 46 (1992).

[2] D. M. Paganin, *Coherent X-ray Optics* (Oxford University, 2006).

[3] M. Ando, A. Maksimenko, H. Sugiyama, W. Pattanasiriwisawa, K. Hyodo, C. Uyama, *Jpn. J. Appl. Phys.* **41**, L1016 (2002).

[4] S. Takagi, *Acta Crystallogr.* **15**(12):1311 (1962).

[5] D. Taupin, *Bull. Soc. Fr. Mineral. Crystallogr.* **87** (1964).

[6] Y. Suzuki, Y. Chikaura and M. Ando, *J. Appl. Phys.* **110**, 084902-1 (2011).

[7] N. Sunaguchi, T. Yuasa, Q. Huo, S. Ichihara, M. Ando, *Appl. Phys. Lett.* **97**(15), 153701 (2010).

[8] S. Ichihara, M. Ando, A. Maksimenko, et al., *Virchows Archiv* **452**(1):41 (2008).

[9] M. Ando, N. Sunaguchi, Y. Wu, S. Do, Y. Sung, A. Louissaint, T. Yuasa, S. Ichihara and R. Gupta, *European Radiology* **23**, 3021 (2013).

msm-ando@rs.noda.tus.ac.jp